

Article

Spectroscopic and Microscopic Correlation of SRO-HFCVD Films on Quartz and Silicon

Haydee Patricia Martínez Hernández ^{1,2}, José Alberto Luna López ^{1,*} ,
José Álvaro David Hernández de la Luz ¹ , Adan Luna Flores ³, Karim Monfil Leyva ¹,
Godofredo García Salgado ¹, Jesús Carrillo López ¹, Rafael Ordoñez Flores ²,
Sergio Alfonso Pérez García ⁴ , Zaira Jocelyn Hernández Simón ¹ ,
Gabriel Omar Mendoza Conde ¹ and Raquel Ramírez Amador ¹ 

¹ Centro de Investigaciones en Dispositivos Semiconductores (CIDS-ICUAP), Benemérita Universidad Autónoma de Puebla (BUAP), Col. San Manuel, Cd. Universitaria, Av. San Claudio y 14 Sur, Edificios IC5 y IC6, Puebla 72570, Mexico; pathaymh@yahoo.com (H.P.M.H.); joalvada1@hotmail.com (J.Á.D.H.d.l.L.); karim.monfil@correo.buap.mx (K.M.L.); godgarcia@yahoo.com (G.G.S.); jesus.jecarril@gmail.com (J.C.L.); imezaira@gmail.com (Z.J.H.S.); gaomec13@gmail.com (G.O.M.C.); newraq77@hotmail.com (R.R.A.)

² Departamento de Ingeniería Eléctrica y Electrónica, Tecnológico Nacional de México/Instituto Tecnológico de Apizaco, Carretera Apizaco-Tzompantepec, esq. con Av. Instituto Tecnológico S/N, Conurbado Apizaco-Tzompantepec, Tlaxcala 90300, Mexico; rafael.ordonezf@gmail.com

³ Facultad de Ingeniería Química, Benemérita Universidad Autónoma de Puebla (BUAP), Av. San Claudio y 14 sur, Edif. FIQ7 C.U., Col. San Manuel, Puebla 72570, Mexico; lunaf86@gmail.com

⁴ Centro de Investigación en Materiales Avanzados S.C. (CIMAV), Alianza Norte 202, Parque de Investigación e innovación Tecnológica Apodaca, Nuevo León 66628, Mexico; alfonso.perez@cimav.edu.mx

* Correspondence: jose.luna@correo.buap.mx; Tel.: +52-222-229-5500

Received: 15 January 2020; Accepted: 11 February 2020; Published: 20 February 2020



Abstract: This work is focused on making a correlation between results obtained by using spectroscopy and microscopy techniques from single and twofold-layer Silicon-Rich Oxide (SRO) films. SRO films single-layer and twofold-layer characterizations were compared considering the conditions as-grown and with thermal treatment at 1100 °C for 60 min in a nitrogen atmosphere. The thickness of the single-layer film is 324.7 nm while for the twofold-layer film it is 613.2 nm; after heat-treated, both thicknesses decreased until 28.8 nm. X-ray Photoelectron Spectroscopy shows changes in the excess-silicon in single-layer SRO films, with 10% in as-grown films and decreases to 5% for the heat-treated films. Fourier Transform Infrared Spectroscopy (FTIR) exhibits three characteristic vibrational modes of SiO₂, as well as, the vibrating modes associated with the Si-H bonds, which disappear after the heat treatment. With UV-Vis spectroscopy results we obtained the absorbance and the absorption coefficient for the SRO films in order to calculate the optical bandgap energy ($E_{g_{opt}}$), which increased with heat-treatment. The energy peaks of the photoluminescence spectra were used to calculate the silicon nanocrystal size, obtaining thus an average size of 1.89 ± 0.32 nm for the as-grown layer, decreasing the size to 1.64 ± 0.01 nm with the thermal treatment. On the other hand, scanning electron microscopy and high-resolution transmission electron microscopy images confirm the thickness of the twofold-layer SRO films as 628 nm for the as-grown layer and 540 nm for the layer with heat-treatment, and the silicon nanocrystal size of 2.3 ± 0.6 nm for the films with thermal treatment.

Keywords: SRO; silicon nanocrystal; HFCVD; PL; HRTEM; XPS

1. Introduction

Currently, technological advances are using sophisticated photoluminescent materials in different science areas. One of these materials is Silicon-Rich Oxide (SRO). This material has evolved since DiMaria et al. [1] observed electroluminescence in SRO for the first time, likewise, Leight Caham [2] by electrochemical etching obtained visible emission of porous silicon. Many topics of research have been investigating to obtain light emitters based on silicon and fully compatible with the existing Complementary Metal Oxide Silicon (CMOS) technology [3–7]. The SRO films have been manufactured by different techniques, the most common being the Chemical Vapor Deposition, such as LPCVD (Low-Pressure Chemical Vapor Deposition) [3,4,8,9], HFCVD (Hot Filament Chemical Vapor Deposition) [10–13], PECVD (Plasma-Enhanced Chemical Vapor Deposition) [14–16], sol-gel [14], silicon implantation in SiO₂ [4,5,8,9], and sputtering [17,18]. All these techniques are compatible with integrated circuits manufacture technology and have given place to several types of applications such as waveguides, non-volatile memories, peak suppressors, light detection, and emission devices. Especially, the SRO deposited by using (HFCVD) and later heat treated (HT) at 1000 °C for 60 min in an N₂ environment has generated a high photoluminescent emission. According to Lin et al. [4], the most luminescent SRO film has an excess of silicon between 5% and 7%. When the excess of silicon is greater than 7%, the emission is faded out and the film is more conductive. Unfortunately, if the excess of silicon is less than 1%, the material tends to be non-stoichiometric silicon oxide and loses its emission properties [5]. In this work, the HFCVD technique was used to deposit SRO films controlling the excess of silicon by means of the flow of molecular hydrogen dissociated at 2000 °C, which strips the sources of quartz to obtain the precursors which are necessary to grow the SRO films. The SRO films formed by one layer and two layers with an excess of silicon between 10% and 5% and with high light emission were obtained. A comparative analysis of the optical, morphological, and structural characterizations are also addressed in order to determine the relationship between X-ray Photoelectron Spectrometry (XPS) and Fourier Transform Infrared Spectroscopy (FTIR) in relation to the oxidation states and the Si-O-Si bonding; the optical band gap energy ($E_{g,opt}$) obtained by using the Photoluminescence (PL) peaks was utilized to estimate the silicon nanocrystals (Si-ncs) size, which was in turn compared with that obtained by High-Resolution Transmission Electron Microscopy (HRTEM). We analyze the influence of the defects and the formation of amorphous and crystalline nanoparticles in as-grown and heat-treated films to understand the PL intensity of SRO films.

2. Material and Methods

Silicon wafers, P-type (100), 2" diameter, low resistivity (1–5 Ω-cm) y 300 microns thickness, were used as substrates for the deposit of SRO films; these substrates were previously cleaned by standard Metal Oxide Semiconductor (MOS) process [12,13]. Quartz (Q) substrates were also used for the deposition of the SRO films, they were cleaned with xylene, acetone, and deionized water before making the deposits. The SRO films were deposited by employing an HFCVD system this system was homemade. In the process, it was used two molecular Hydrogen fluxes (H₂) at levels of 25 and 100 sccm. Two single-layer structures labeled as SRO₂₅ and SRO₁₀₀, and two twofold layer ones SRO_{25/100} and SRO_{100/25} were grown. The molecular Hydrogen flux is dissociated at 2000 °C in 11 filaments energized at 74 volts with a current of 38.4 amperes, which shifts to highly reactive atomic hydrogen, stripping 11 quartz sources placed under the incandescent filaments at a distance (dff) from 6 mm, obtaining the volatile precursors, which are deposited and adsorbed on the surface of the hot substrate, which is located under the quartz sources at a distance (dfs) of 8 mm [8,12,13]. The time of deposit (td) for the deposited single-layers was 3 min, and for the twofold-layers, it was 5 min. These parameters of distance and time remained constant for all the deposited SRO films [8,10–13]. After deposition SRO films were heat-treated at 1100 °C for 60 min in a Nitrogen (N₂) environment. The thickness and refractive index of SRO films deposited on Si substrates both as-grown (as-G) and with heat-treated (HT) were characterized by Ellipsometer (Gaertner L117 model, San José, CA, USA). With a laser He-Ne of 632.8 nm wavelength. High-resolution X-ray photoelectron spectroscopy (XPS), (PHI ESCA-5500

model, 18725 Lake Dr E, Chanhassen, MN, USA). Measurements were done to determine the silicon content of the samples using a Thermo Scientific Escalab 250Xi instrument. The base pressure during the analysis was $\sim 10^{-10}$ mbar and the photoelectrons were generated with the AlK α (1486.68 eV) X-ray source, using a monochromator, and a spot size of 650 μm . The X-ray voltage and power were 14 kV and 350 W, respectively. The acquisition conditions for the high-resolution spectra were 20 eV pass energy, 45° take-off angle and 0.1 eV/step. SEM (JEOL-JSM-7800F model, 3-1-2 Musashino, Akishima, Tokyo, Japan) was used to observe the interfaces of the SRO films. FTIR spectra of the SRO films were obtained with Bruker Vector 22 Spectrophotometer with an infrared source (Bruker Vector 22 model, Virginia, WV, USA); the measurements were obtained in the range from 400 to 2400 cm^{-1} with a resolution of 4 cm^{-1} .

All measurements were performed using the above conditions in an ultrahigh vacuum of 4×10^{-10} mbar. Transmission and absorption spectra of the SRO films deposited on Q were obtained by using the UV-Vis equipment, (Perkin Elmer model Lambda 3b 5910 Midway Park Blvd NE #5900, Albuquerque, NM, USA) from 200 to 900 nm. Photoluminescence spectra of SRO films were measured using the Fluoromax-3 spectrofluorometer, (Horiba Jobin Yvon model, 2, Miyanohigashi-cho, Kisshoin Minami-Ku Kyoto, Japan) at room temperature for which an excitation line of 300 nm was used and the emission signal was collected in the range from 400 to 900 nm. Transmission Electron Microscopy (TEM) (JEM-ARM200F model, Tokyo, Japan), was used to corroborate the presence of silicon nanocrystals at the Si-SRO interface.

3. Results

Table 1 shows the parameters used to deposit the single-layer films (SRO₂₅ and SRO₁₀₀) and twofold-layers (SRO_{25/100} and SRO_{100/25}). The thickness (Th) and refractive index (η_{SRO}) were obtained by null ellipsometry and the Silicon excess was measured by XPS of the as-G and HT SRO films. Table 1 also displays the values of the as-G and HT SRO films thickness; as can be seen, all the HT SRO films exhibited a decrease in their thickness respect to that of the as-G films. This fact is due to the microstructural rearrangement of the films, as well as the desorption of Hydroxyl (OH) and Hydrogen (H) in Si-H species that were not well bonded to the SRO films and the formation of silicon nanocrystals (Si-ncs) and Si-nanoclusters. This generated a change in the material stoichiometry, which led the material approaches the SiO₂, as it will be seen in short in the FTIR spectra. From this Table 1, it was also observed that the as-G SRO₂₅ and SRO₁₀₀ films had a refractive index of $\approx 2.24 \pm 0.21$, which is closer to the refractive index of Silicon ($\eta_{\text{Si}} \approx 3$ to 4) [14], indicating that such films contained a high silicon excess. This is corroborated by the XPS measurement, which gave 9.9% and 10.6% in the profiles of silicon for SRO₂₅ and SRO₁₀₀ films, respectively. That was observed in Figure 1a,c, where the silicon excess was obtained of the ratio of the stoichiometric SiO₂, where the composition was silicon (33%) and Oxygen (66%). Then in Figure 1a, the value of silicon for SRO was 42.9% with respect to SiO₂ we had a silicon excess of $42.9\% - 33\% = 9.9\%$. These single-layer HT SRO films had a smaller refractive index, of approximately 1.3 ± 0.06 showing a tendency to the refractive index of SiO₂ ($\eta_{\text{SiO}_2} \approx 1.4$) [5,15,16], likewise, in the same films, the silicon excess decreased to 5.5%, according to the profiles of silicon stable throughout the thickness, which were observed in Figure 1b,d. Furthermore, in the twofold-layer SRO_{25/100} and SRO_{100/25} films the refractive indexes show an inverse behavior to the single-layers because they tended to increase, approaching to the refractive index of Si, indicating that the silicon excess atoms contained in the microstructure of the film underwent a structural rearrangement, tending towards a structure of SiO₂, this was observed in Table 1. In the refractive index parameters, there was no dependence on the substrate used (Q and Si).

Table 1. Parameters of manufacture, labeling thickness (Th) and refractive index of the Silicon-Rich Oxide (SRO) films (η_{SRO}) as-grown (as-G) and heat-treated (HT).

Film	d_{ff} mm	d_{fs} mm	T_{d} mins	as Grown				Heat-Treated					
				Sample	Th nm	η_{SRO}	Silicon Excess %	Sample	Th nm	η_{SRO}	Silicon Excess %		
25	6	8	3	Si/SRO ₂₅	322.9	2.46 ± 0.03	9.9	Si/SRO ₂₅	296.3	1.3 ± 0.04	5.5		
				Q/SRO ₂₅	334.7			Q/SRO ₂₅	311.2				
100				Si/SRO ₁₀₀	319.6	2.039 ± 0.35	10.6	Si/SRO ₁₀₀	283.5			1.02 ± 0.08	5.0
				Q/SRO ₁₀₀	314.7			Q/SRO ₁₀₀	293.1				
25/100			5	Si/SRO _{25/100}	592.3	1.46 ± 0.06	Si/SRO _{25/100}	583.3	1.93 ± 0.31				
				Q/SRO _{25/100}	647.5			Q/SRO _{25/100}		591.6			
100/25				Si/SRO _{100/25}	578.9	1.51 ± 0.02		Si/SRO _{100/25}	560.5	2.05 ± 0.65			
				Q/SRO _{100/25}	639.8			Q/SRO _{100/25}	594.0				

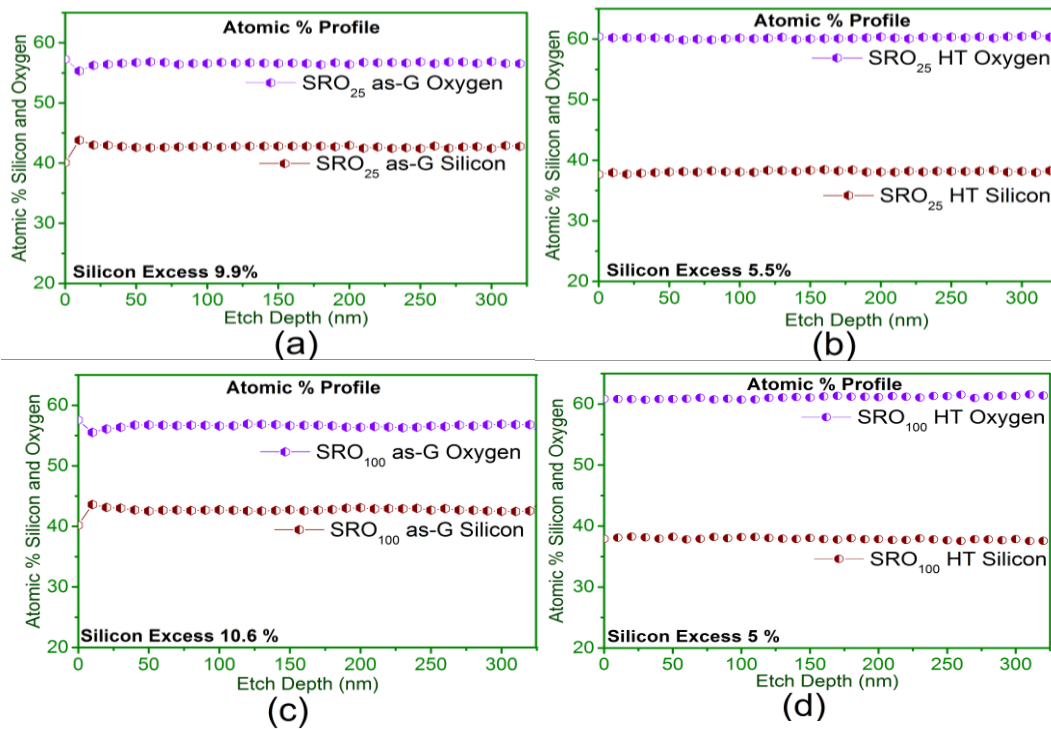


Figure 1. Silicon excess in single-layer SRO₂₅ and SRO₁₀₀ films (a) and (c) as-G and (b) and (d) with HT.

Figures 2 and 3 show the behavior of the XPS Si2p spectra of the single-layer films SRO₂₅ and SRO₁₀₀ taking into account both as-G and HT conditions where the binding energies are located in the energy region from 99 to 104 eV [14–19]. In Figures 2 and 3a–c for the SRO₂₅ and SRO₁₀₀ films, the energy peaks were located at 99.3, 99.4, and 99.7, 100.7, and 100.2, 101.2, 101.4, and 101.5, 102, 102.1, 102.5, and 102.8, 103, 103.1, 103.2, 103.3, 103.4, 103.7, and 103.8 eV in conditions as-G, attributed to the oxidation states Si⁰⁺, Si⁰⁻ (Si), Si¹⁺, Si²⁺, Si³⁺, and Si⁴⁺ (SiO₂), respectively; those energy peaks in the proximity of 99 eV, indicate that in this energy region there is a greater amount of Si.

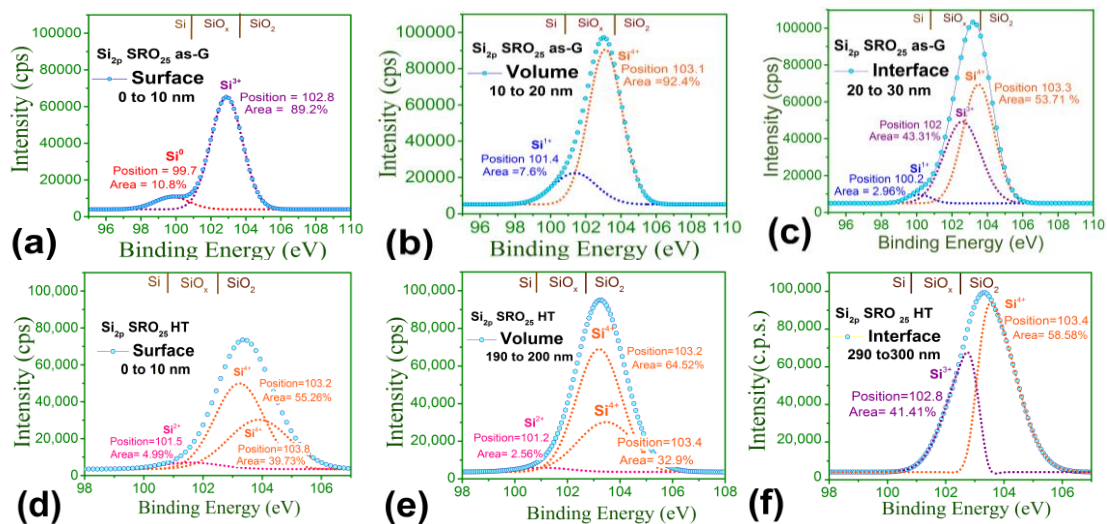


Figure 2. XPS spectra of Si_{2p} of single-layer films of SRO₂₅ (a), (b) and (c) as-G and (d), (e) and (f) with HT, with different oxidation states on the surface, in the volume, and at the SRO/Si interface.

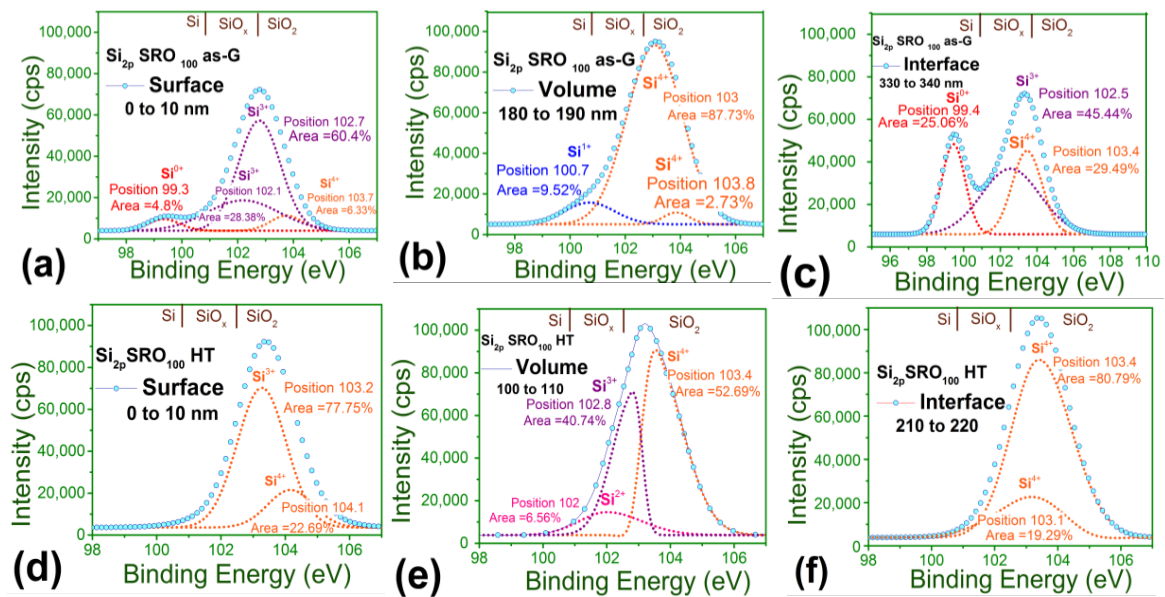


Figure 3. XPS spectra of Si_{2p} of single-layer films as-G and HT SRO_{100} , with different oxidation-states, (a) and (d) on the surface, (b) and (e) in the volume, and (c) and (f) at the SRO/Si interface.

On the other hand, in Figures 2 and 3d–f we could see that the energy peaks corresponding to the SRO_{25} and SRO_{100} HT films on the surface, in the volume and on the SRO/Si interface were observed in the vicinity of ≈ 103 eV, which indicates that there is a thin layer of SiO_2 (Si^{4+}) in such structures. According to the binding energies (101, 102, 103, and 104 eV) of the films HT SRO_{25} and SRO_{100} shown in Figures 2 and 3d–f, it is inferred that the four different oxidation states Si^{1+} , Si^{2+} , Si^{3+} , and Si^{4+} were present in these structures; it is in agreement with Chen [17]. Additionally, the Si_{2p} peak of SiO_x contained five components corresponding to a non-oxidized state Si^0 and four different silicon oxidation states, which were present in our HT films, this means that the Si-Si bonds were replaced by Si-O bonds (Si_4O , Si_3O_2 , Si_2O_3 , and SiO_4). Therefore, it was concluded that there was a separation of phases as indicated by the presence of the energy peaks of Si and SiO_2 , whose energy values are shown in Table 2.

Table 2. Oxidation phases of SRO_{25} and SRO_{100} single-layer films analyzed by XPS.

SRO	Film Location	Oxidation Phases Peak Position (eV)				
		Si^0	Si^{1+}	Si^{2+}	Si^{3+}	Si^{4+}
25 _{as-G}	Surface	99.7			102.8	
25 _{HT}				101.5		103.2, 103.8
100 _{as-G}		99.3			102.1, 102.7	103.7
100 _{HT}						103.2, 104.1
25 _{as-G}	Volume			101.4		103.1
25 _{HT}				101.2		103.2, 103.4
100 _{as-G}			100.7			103, 103.8
100 _{HT}					102 102.8	103.4
25 _{as-G}	SRO/Si		100.2		102	103.3
25 _{HT}					102.8	103.4
100 _{as-G}					102.5	103.4
100 _{HT}						103.1, 103.4

The micrograph obtained from the twofold-layer Si/ $\text{SRO}_{25/100}$ structure is shown in Figure 4. Both (a) as-G and (b) with HT, where the film thickness was 320 nm for the $\text{SRO}_{25\text{as-G}}$ film and 308 nm for the $\text{SRO}_{100\text{as-G}}$ film. In the same way, it was 300 nm and 240 nm for the $\text{SRO}_{25\text{HT}}$ film and the $\text{SRO}_{100\text{HT}}$

film, respectively. All these values were corroborated with those obtained by null spectroscopy being both values very approximate, as shown in Table 1.

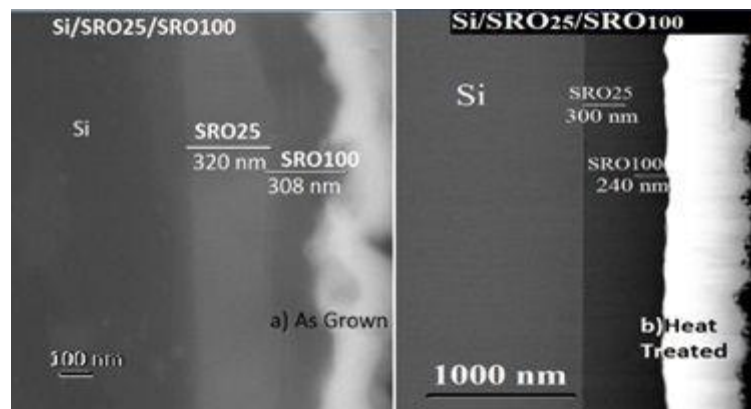


Figure 4. Scanning Electron Microscopy (SEM) of the Si/SRO_{25/100} structure as grown and with HT.

In Figure 5, the FTIR absorption spectra obtained from the single-layer and twofold-layer films of SRO₂₅, SRO₁₀₀, SRO_{100/25}, and SRO_{25/100} deposited on Silicon substrates are shown, therein we could observe the different bands and intensities of the vibrational modes corresponding to the Rocking ($R = 458 \text{ cm}^{-1}$), Bending ($B = 812 \text{ cm}^{-1}$), and Stretching in-phase ($S = 1084 \text{ cm}^{-1}$) and out of phase ($a-S = 1177 \text{ cm}^{-1}$) of Si-O-Si bonds; these bands are characteristic of SiO₂ [10,11,18,19]. Additional vibrational modes with lower absorption intensity are identified such as the band at 620 cm^{-1} , which is due to vibrations Si-H (Wagging) [20,21]. In addition, vibrations around 2250 and 2350 cm^{-1} , which correspond to the asymmetric stretching bonds of Si-H ($S = 2260$ or 2358), are shown [9,20]. The spectra of Figure 5 along with their intensity can be correlated with the data in Table 1, where the increase in the intensity of the absorbance band of the vibrational modes is modulated by the SRO film thickness, so that if the thickness of the film increases, the intensity and the average width of the band of the vibrational mode will also increase, indicating higher density of Si-O-Si bonds. The SRO films with HT exhibit that there is an increase in the intensity of the absorption bands with respect to those with no HT, as can be seen in (1), (2), (3), (4), (5), and (6) of Figure 5, which show a shift in the wavenumber, due to the modification of the stoichiometry for each SRO film, where the composition of the SRO films is modified as has already discussed in the XPS results. The boxes (2), (3), (6), and (7), show in detail the Si-H (620 cm^{-1}), Si-OH (880 cm^{-1}), Si-OH (2250 cm^{-1}), and Si-OH ($3380\text{--}3850 \text{ cm}^{-1}$) bonds, which were present in the films in consequence of the incorporation of Hydrogen in the experimental process. It should be noted that with heat-treated the bands (2) and (7) decreased and the bands (3) and (6) disappeared, due to the hydrogen desorption at high temperatures.

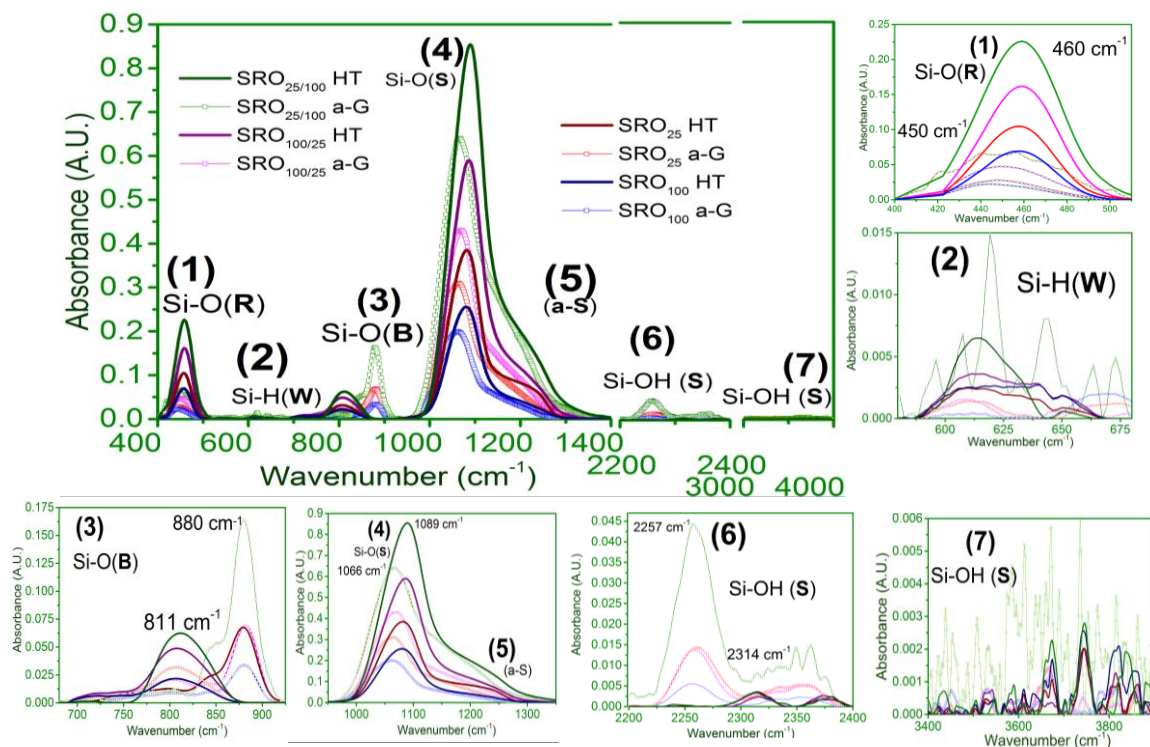


Figure 5. Spectra of the FTIR of the $\text{SR}_{0.25}$, $\text{SR}_{1.00}$, $\text{SR}_{0.25/1.00}$, and $\text{SR}_{1.00/0.25}$ films, as-G and HT deposited on silicon substrates.

Table 3 shows the vibrational modes of SiO_2 and the SRO films under the conditions as-G and HT for making comparisons. The frequency bands of the vibrational modes (R, B, and S) as-G were localized in lower wavenumbers than those of the SiO_2 , which indicates that the oxide was non-stoichiometric due to the increment of the Si-O bonds out of stoichiometry. It is also noticeable the inverse relationship among the position of the stretch band in-phase (4) and the refractive index and the thickness of the film, that is, if the band wave number was lower, then the refractive index and the thickness increase, taking into account only the single-layer SRO films as-G. When thermal annealing was applied these spectra shift to a region of higher wavenumber than that of SiO_2 and were attributed to a structural rearrangement and improved stoichiometry, due to the phase separation of Si and SiO_2 . It could be observed in (4) of Figure 5, the difference in the positions of the main bands of the (S) band, where a shift towards higher wavenumbers were observed for the HT films, being the spectrum of the film $\text{SR}_{0.25/1.00}$ the one that suffered the biggest change when moving its maximum point from 1066 to 1089 cm^{-1} , in addition to the increase in the absorbance intensity to a high value and the narrowing of the spectrum for the same films; these changes indicate the degree of deviation of the stoichiometry, that means that some of the oxidation states of the SiO_x network, which was formed by the tetrahedron Si- ($\text{Si}_4\text{-n-On}$) with $n = 0, 1, 2, 3$, and 4, forming: Si^0 , Si^{1+} , Si^{2+} , Si^{3+} , and Si^{4+} , varied according to the excesses of silicon and the time of deposit of the film, where the processes of absorption, diffusion and desorption occur [10,22]. According to Koshida [23], the vibration modes Si-H flexion (875 cm^{-1}) and Si-H stretch (2260 cm^{-1}) are present in the films due to the incorporation of Hydrogen in the manufacturing process. However, in HT films, the Hydrogen desorption leads these bands to disappear due to the heat-treated carried out at high temperatures.

Table 3. IR vibration bands of the SiO_x as-G and HT SRO films.

Vibrational Modes	As Grown				SiO ₂	Heat-Treated			
	S ₂₅	S ₁₀₀	S _{100/25}	S _{25/100}		S ₂₅	S ₁₀₀	S _{100/25}	S _{25/100}
	Wave Number cm ⁻¹								
(1) Si-O-Si in SiO ₂ Rolling (R) [13–16,20–22]	450	449	448	449	458	459	457	458	459
(2) Si-H Wagging (W) [17,23]	610	612	612	619		616	620	625	614
(3) Si-O-Si in SiO ₂ Bending (B) [13–16,20–22]	801	799	802	797	812	812	812	811	811
(3) Si-OH Bending (B) [13–16,20–22]	880	881	880	880		879	806	808	810
(4) Si-O-Si in SiO ₂ Stretching in-phase (S) [13–16,20–22]	1066	1064	1062	1068	1082	1084	1082	1080	1088
(5) Si-O-Si Stretching out of phase (a-S) [13–16,20–22]	1163	1154	1168	1175	1177	1208	1192	1227	1230
(6) Si-OH Stretching (S) [17,18]	2258	2259	2258	2258		2315	2316	2315	2314
(7) Si-OH Stretching (S) [17,18,23]	3669	3670	3743	3667		3744	3742	3813	3742

Figure 6 shows the transmittance spectra from the as-G films deposited on a quartz substrate; it was observed that for the case of the SRO₂₅, SRO_{100/25}, and SRO_{25/100} films, they exhibited a transmittance greater than 85% in the optical range 500–900 nm; however, the SRO₁₀₀ film exhibited a lower transmittance of the order of 60–80% in this optical range. It was emphasized that their transmittance absorption edge was located in the violet range (300–400 nm), in addition, such edge moved as the SRO film thickness was varied. Whereas for the HT SRO film the transmittance exceeded 85% and a shift of the absorption edge towards the far UV was observed from 200 to 300 nm, at shorter wavelengths. Besides the absorption intensity was weaker because the dispersion effect of light was reduced as a consequence of the structural rearrangement, which provoked a reduction of the defects density and the phase separation in the material. It should be noted that the change in the transmittance threshold was due to the corresponding change of the absorption coefficient edge, as shown in the insets in Figure 6, which ranged approximately from 3.2 to 3.8 eV for the as-G SRO films, which possessed a higher silicon excess, while from 4.2 to 5.8 eV for the HT SRO films, which underwent a decrement of the silicon excess, this effect is reported by Zacharias [24], besides the smaller the silicon excess, the smaller Si-ncs size. This fact led to the increase of the energy bandgap of the films, as could be corroborated in Table 4. Well-formed Si-ncs of 2.3 ± 0.6 nm on average size were found by HRTEM as shown in Figure 7, this is in accordance with that reported by Zacarias [24]. The insets in Figure 6 show the spectra of the absorption coefficients corresponding to both as-G and with HT films, where the absorption edge moved towards shorter wavelengths when the silicon excess decreased (HT films) and it was more noticeable in the single-layer films deposited on Quartz, especially in the SRO₁₀₀ film, which had its absorption edge ranging from 3 to 4 eV under as-G condition and it shifted to higher energies from 5 to 6 eV under HT condition, this effect is considered in some works [25–27] and it is attributed to a wide distribution in small size amorphous silicon quantum dots; therefore, the SRO₂₅ and SRO₁₀₀ films have silicon crystalline and amorphous nanoparticles being the latter in greater quantity for the SRO₁₀₀ film.

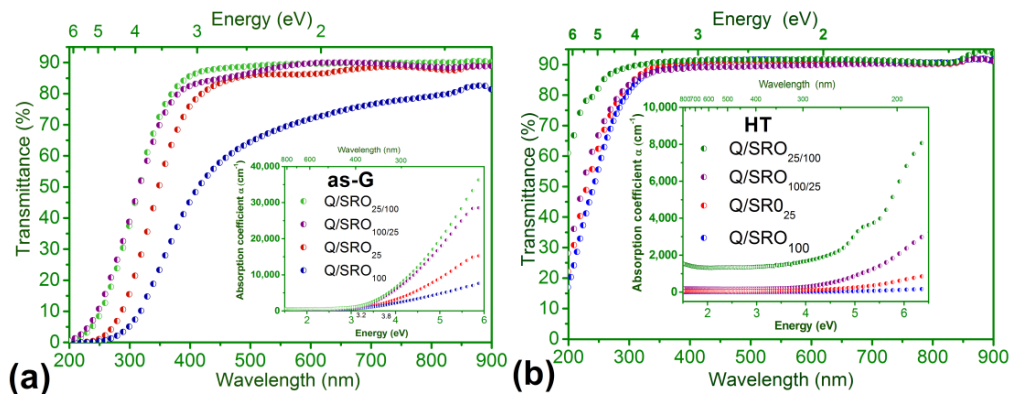


Figure 6. The transmittance of the SRO₂₅, SRO₁₀₀, SRO_{25/100}, and SRO_{100/25} films, (a) as-G and (b) with HT.

Table 4. Theoretical values of the $E_{g_{opt}}$ and diameter of the Si-ncs calculated with the Tauc plot of the SRO films.

Sample	As-Grow		H-T	
	$E_{g_{opt}}$ (eV) of the SRO Films	Diameter (d) of the NC-Si (nm)	$E_{g_{opt}}$ (eV) of the SRO Films	Diameter (d) of the NC-Si (nm)
QSRO ₂₅	2.90	1.75	3.00	1.68
QSRO ₁₀₀	2.50	2.13	2.97	1.65
QSRO _{25/100}	2.95	1.72	3.38	1.47
QSRO _{100/25}	2.85	1.79	2.90	1.75

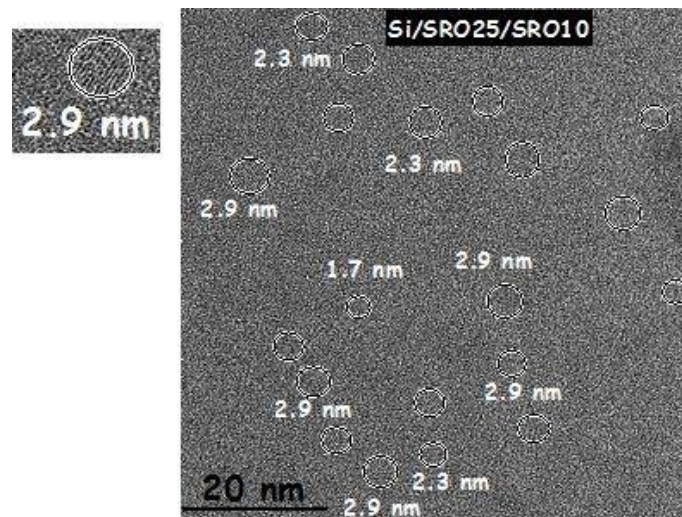


Figure 7. Micrographs of the structure Si/SRO₂₅/SRO₁₀₀ in the High-Resolution Transmission Electron Microscopy (HRTEM) mode of the SRO films deposited by the Hot Filament Chemical Vapor Deposition (HFCVD) technique, it shows the Si-ncs size (circles).

The absorption coefficient (α) was obtained from the transmittance, through the Tauc relation [26]. Subsequently with the mathematical relationship [28,29]:

$$(\alpha h\nu)^{1/n} = C_1 (h\nu - E_{g_{opt}}) \tag{1}$$

Acronyms are defined as follows: $E_{g_{opt}}$ is the optical band gap energy for the different films, C_1 is a constant of proportionality that is independent of the photon energy ($C_1 \approx 1$) [8,25,30], ν is

the light frequency, and n characterizes the nature of the band transition type. In these films, a value of $n = 3$ was determined because we had an indirect forbidden transition due to the strong influence of the Si-ncs, which are also cited for the SRO [23]. The $E_{g_{opt}}$ of the SRO films is shown in Figure 8, where the size of the Si-ncs plays a key role in the value of the same.

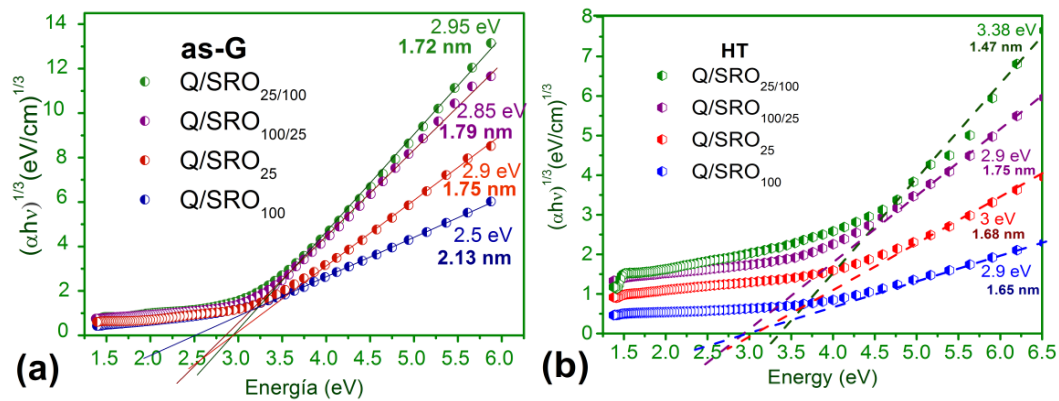


Figure 8. Optical bandgap energy of the SRO films (a) as-G and (b) with HT.

With the experimental values of the $E_{g_{opt}}$ it is possible to estimate the Si-ncs size (d = Si-ncs diameter) using Equation (2) [28], thus the calculated diameters are shown in Table 4 together with the corresponding $E_{g_{opt}}$ of each film.

$$d = \left[\frac{3.73}{E_{g_{opt}} - 1.12} \right]^{\frac{1}{1.39}} \quad (2)$$

The data in Table 4 show the $E_{g_{opt}}$ of the SRO films deposited on Q substrates. The as-G SRO₂₅, SRO₁₀₀, SRO_{25/100}, and SRO_{100/25} films present an $E_{g_{opt}}$ of 2.90, 2.50, 2.95, and 2.85 eV, respectively, which contrast strongly with that of the Si $E_{g_{opt}}$, which is 1.12 eV [9,25,28,29], because of the presence of the Si-ncs. For SRO₂₅, SRO₁₀₀, SRO_{25/100}, and SRO_{100/25} films with HT, the $E_{g_{opt}}$ increased slightly beginning at 2.90 up to 3.38 eV, respectively, as a consequence of a restructuring of the Si-ncs that reduced their dimensions and increased their bandgap due to dimensional quantum confinement. Therefore, the light absorption process was influenced by the Si-ncs and Si-nps and the defects that are immersed in the SiO_x matrix inducing that the absorption to be in the UV range [23,24]. Additionally, the absorption processes were also influenced by the change of silicon excess, which gave rise to the formation of silicon islands and Si-ncs when the films were subjected to the heat-treated. Particularly, it was observed that the silicon excess in SRO₁₀₀ films produced very small amorphous nanoparticles (1.5 nm) modeling this material as dispersed Si and O atoms, producing mainly defects and a high structural disorder [31]. Figure 7 shows the micrographs obtained by the HRTEM technique for the case of the SRO_{25/100} films therein we could see the Si-ncs (circles) that were mainly responsible for the photoluminescence observed in this structure, the circles emphasize the size of the Si-ncs and the inset shows an enlargement of the crystalline orientation of the Si-ncs formed. The HRTEM micrographs were analyzed by means of the Digital Micrograph program, using the Fourier transform to obtain the reciprocal space and identify the size of the Si-ncs, the crystallographic planes, and the interplanar distance in order to corroborate the Si-ncs existence. Through these micrographs, we obtained the average diameter of the Si-ncs resulting in 2.3 ± 0.6 nm for the SRO_{25/100} film.

On the other hand, Figures 9 and 10 show the photoluminescent (PL) emission spectra of the single-layer SRO films and Figures 11 and 12 show the twofold-layers SRO films, both on Quartz and Silicon substrates, as-G and with HT. In the graphs of Figures 9, 10, 11 and 12a,b, are showing the PL spectra as they were just obtained to compare the intensity PL as-G and with HT, while in the insets of Figures 9, 10, 11 and 12c,d, the spectra were plotted according to the Energy $I(E) dE$ versus

the energy ratio given by Y. Wang and PD Townsend [32], to obtain the graphs in terms of energy and perform the deconvolutions that determine the most intense energy peaks and thus relate them with the emission mechanisms. It is emphasized that the evolution of the peaks in the PL spectra both in their intensity and in the wavelength shifted from their position is attributed mainly to the heat-treated carried out at 1100 ° C for 60 min in N₂ atmosphere. Therefore, the thermal treatment significantly affects not only the intensities of the peaks in the PL spectra but also their width and position at the corresponding wavelength.

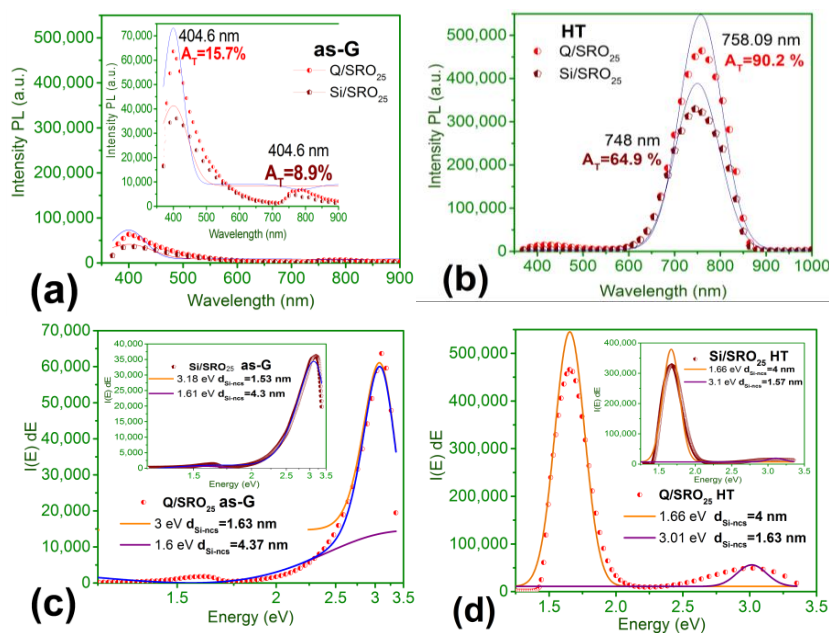


Figure 9. Photoluminescence of the single-layers SRO₂₅ films deposited by the HFCVD system under conditions (a) and (c) as-G and (b) and (d) with HT.

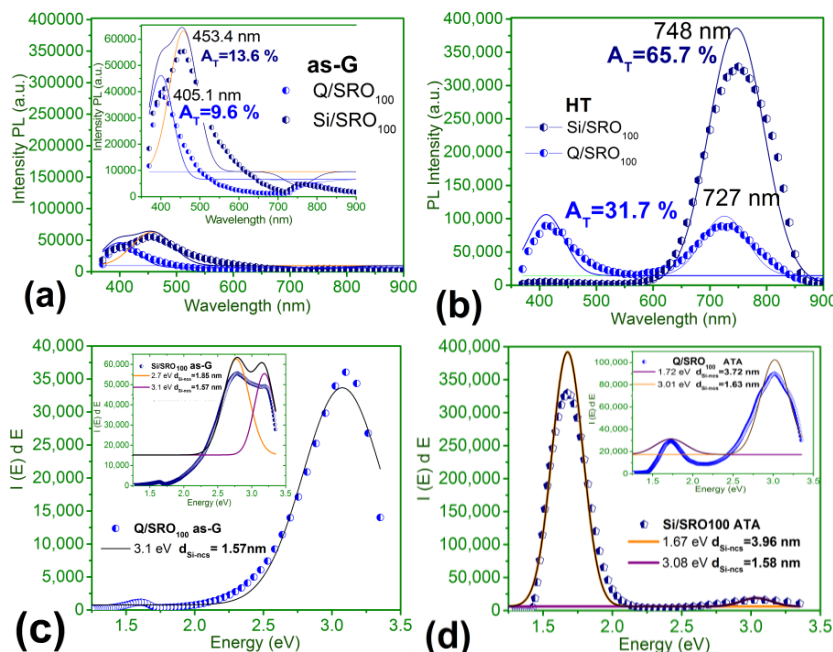


Figure 10. Photoluminescence of the SRO₁₀₀ films deposited by the HFCVD system under conditions (a) and (c) as-G and (b) and (d) with HT.

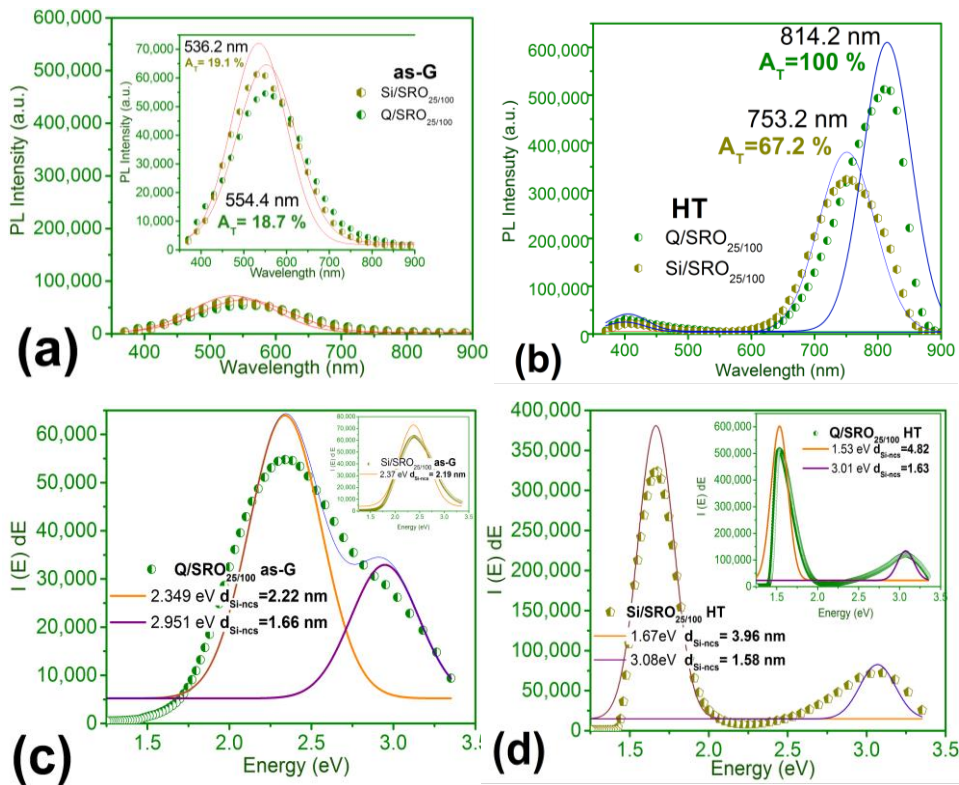


Figure 11. Photoluminescence of the $SRO_{25/100}$ films deposited by the HFCVD system under conditions (a) and (c) as-G and (b) and (d) with HT.

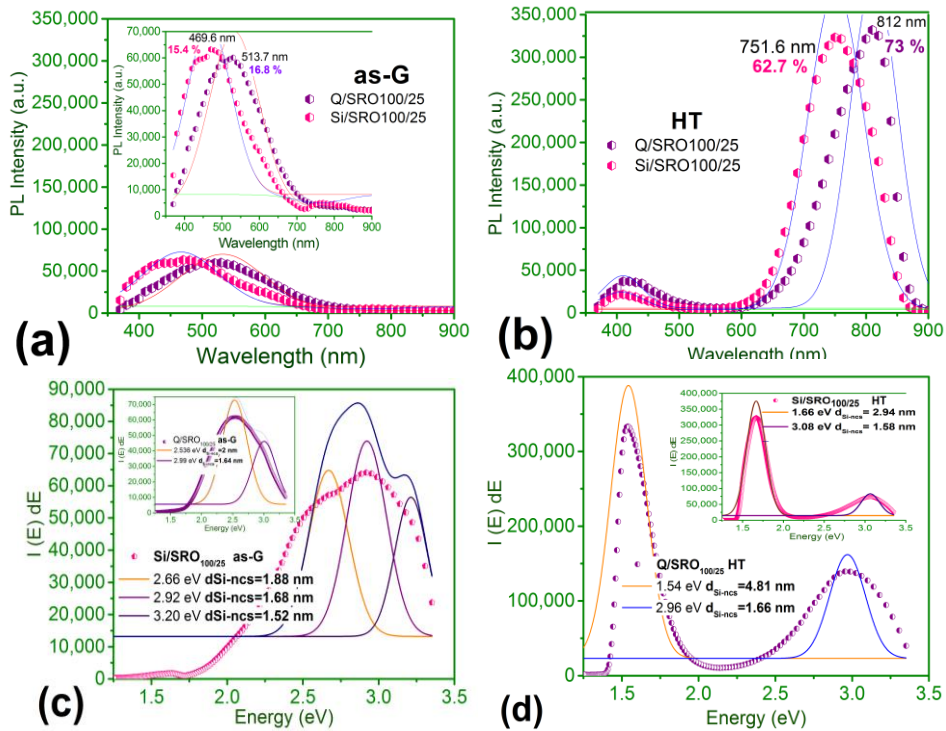


Figure 12. Photoluminescence of the $SRO_{100/25}$ films deposited by the HFCVD system (a) and (c) as-G and (b) and (d) with HT

From all the PL spectra depicted by Figures 9–12, it is evident that their intensity, width and peak position were strongly dependent on the quartz and silicon substrate used in the deposit of the SRO films. We stressed that the total area (A_T) of the deconvolutions associated with the PL spectrum is shown to clarify the PL intensity as shown in the upper graphs (a and b) in Figures 9–12. It is worthy to note that the thermal treatment not only strengthened the PL intensity but also shifted the position of the peak in such a way that two bands of emission were well defined of the SRO films. In Tables 5 and 6, values of the PL intensities, optical band gap energies, and nanocrystal diameters are listed, both as-G and HT for the two types of substrate in order to make comparisons. Note that the SRO as-G films possess in general a reduced PL intensity in the bands: violet, blue, green, yellow, and orange. The physical origin of this phenomenon is the presence of a very high concentration of Hydrogen in the SRO film and when the heat-treatment is applied at 1100 °C for 60 min, the Hydrogen escapes from the film, hence the violet-yellow PL band disappears, but the red band increases its PL intensity remarkably.

Table 5. Estimated values of the E_{gopt} and diameters of the Si-ncs calculated by the absorbance of the SRO films.

Sample	Position	Intensity	Nanocrystal Diameter (nm)		Sample	Intensity	Nanocrystal Diameter (nm)		
			PL	Tauc			PL	Tauc	
as-G	E_{gopt} (eV)	(c.p.s.)	PL	Tauc	HT	E_{gopt} (eV)	(c.p.s.)	PL	Tauc
Q25	3.00	63,951	1.63	1.85	Q 25	1.63	466,185	4.18	
Q25	1.6	2,620	4.37		Q25	3.01	54,319	1.63	1.70
Si 25	3.18	36,152	1.53		Si 25	1.66	326,662	4.00	
Si 25	1.61	1,649	4.30		Si 25	3.1	18,661	1.57	
Q 100	3.1	36,414	1.57	1.62	Q 100	1.72	29,486	3.72	
Si100	2.7	55,654	1.85		Q 100	3.01	90,844	1.63	1.65
Si100	3.1	49,129	1.57		Si 100	1.67	329,163	3.96	
Q 25/100	2.34	54,536	2.22	2.43	Q 25/100	1.53	511,742	4.82	
Q 25/100	2.95	28,750	1.66		Q 25/100	3.01	129,289	1.63	1.49
Si 25/100	2.37	663,686	2.19		Si 25/100	1.67	327,345	4.81	
Q 100/25	2.53	61,786	2.00	1.85	Si 25/100	3.08	83,362	1.58	
Q 100/25	2.99	42,253	1.64		Q 100/25	1.54	333,988	4.81	
Si 100/25	2.66	57,715	1.88		Q 100/25	2.96	140,599	1.66	1.70
Si 100/25	2.92	64,215	1.68		Si 100/25	1.66	327,291	2.94	
Si 100/25	3.2	49,325	1.52		Si 100/25	3.08	77,253	1.58	

Table 6. Position, intensity, and percentage of the total area of the photoluminescence spectra.

Samples		As-Grow		Sample		Heat-Treated	
Substrates	Position (nm)	Intensity (A.U.)	A_T (%)	Substrates	Position (nm)	Intensity (A.U.)	A_T (%)
Si/SRO25/100	536.2	61,574.7	19.1	Q/SRO25/100	814.2	509,139.7	100.0
Q/SRO25/100	554.4	54,882.6	18.7	Q/SRO25	758.09	462,931.5	90.2
Q/SRO100/25	513.7	61,914.2	16.8	Q/SRO100/25	812	332,546.4	73.0
Q/SRO25	404.6	63,951.6	15.7	Si/SRO25/100	753.2	324,098.8	67.2
Si/SRO100/25	469.6	61,965.4	15.4	Si/SRO100	748	330,469.0	65.7
Q/SRO100	453.4	54,617.9	13.6	Si/SRO25	509.9	327,256.6	64.9
Si/SRO100	405.1	39,220.4	9.6	Si/SRO100/25	751.6	323,288.0	62.7
Si/SRO25	404.6	63,808.1	8.9	Q/SRO100	727	91,324.5	31.7

The energy function graphs are shown in the lower graphs (c and d) in Figures 9–12, the extracted deconvolutions exalted the contributions of the different bands contained in the spectrum, which in turn defined the different mechanisms of emission, which produced the PL phenomenon. Table 5 lists

the $E_{g_{opt}}$ values of the highest peaks of the PL spectra, which are used by Equation (2), to estimate the Si-ncs diameter. For the SRO₂₅ and SRO₁₀₀ as-G films we found the same 3.01 eV $E_{g_{opt}}$, which corresponds to a 1.8 nm Si-ncs diameter, the results are listed in Table 5; there some values of the Si-ncs diameters were compared with those obtained by the Tauc method.

On the other hand, it is observed in Figure 9a,c and Figure 10a,c that the as-G single-layer films exhibited different PL intensities highlighting the fact that the width and position of the PL peaks did not vary significantly, the reason why this happens is the influence of the substrate type used in the deposit, thus, the as-G SRO₂₅ and SRO₁₀₀ films deposited on Q substrate present a higher PL intensity than that corresponding to the films deposited on Si substrate. However, these structures with HT show outstanding changes as can be seen in Figures 9 and 10b,d; because the SRO₁₀₀ HT films deposited on Q substrate and on Si substrate, the former spectrum in Figure 10b,d shows two peaks with different intensity without exceeding the order of magnitude of the same as-G SRO₁₀₀ film, the highest PL emission was found in 3 eV (in the violet region), which was attributed to Weak Oxygen Bonds (WOB \approx 3.17 to 2.72 eV) [8–13,22]. The latter spectrum had its emission peak in the red region (1.99–1.77 eV), attributed to the QC with interaction at the Si-ncs -oxide matrix interface, the PL intensity in this region is an order of magnitude greater than that of the SRO₁₀₀ as -G film. The highest PL emission was observed in the HT SRO₂₅ films deposited on the Q substrate with a Total Area percentage under the curve of 90.2%, in the near-infrared (1.77–1.24 eV) [21,22] ascribed to luminescent centers located at the Si-ncs/SiO₂ (CLI) interface. According to Equation (2), the Si-ncs diameter size obtained was about \approx 4 nm in this PL peak.

The twofold-layers, as-G SRO_{25/100}, and SRO_{100/25} deposited on Q and Si substrates are shown in Figures 11 and 12a,b. The spectra of these as-G films were similar both in their shape and PL intensity and the emission region lay mainly in all the visible bands from red to violet (from 1.7 to 3.25). The as-G SRO_{25/100} and SRO_{100/25} films deposited on Q and Si substrates are shown in Figures 11 and 12a,b. Their PL spectra did not exhibit substantial differences both in shape and intensity and the emission region ranges from red to violet (from 1.7 to 3.25 eV), which is attributed to the following luminescent mechanisms: QC, NBOHC, Centers $E' \equiv Si-O \bullet O \equiv Si +$, $E\delta'$, NOV, and WOB. In Table 7 the emission regions and their corresponding mechanisms of emission are listed. Regarding the HT twofold-layer films, the PL spectra presented a close similarity. Concerning the films Q/SRO_{25/100} HT and Q/SRO_{100/25} HT, the PL intensity increased an order of magnitude and the emission bands were located in the near-infrared region (1.52 eV) and was attributed to luminescent centers located at the interface of Si-ncs/SiO₂ (CLI \approx 1.77–1.24 eV) [22,33]. In this case, the Si-ncs diameter size was 4.82 nm for this PL peak. In addition, it was found a second PL emission located at \approx 3 eV, which was due to weak oxygen bonds (WOB), and the Si-ncs diameter size was about 1.6 ± 0.025 nm. The Si/SRO_{25/100} HT and Si/SRO_{100/25} HT films show a small increase in the PL intensity. However, it was an order of magnitude higher than that exhibited by the same as-G twofold-layer films. This emission band lay in the red one (1.99–1.77 eV), this is caused by the QC effect with an interaction at the Si-ncs-oxide matrix interface, although a considerable emission was also observed in 2.96 eV, corresponding to weak oxygen bonds (WOB), additionally, the Si-ncs size for these twofold-layer HT films corresponding to a low-energy band was \approx 5 nm, and to a high energy band was \approx 1.66 nm; all this could be observed in Figure 11b,d and Figure 12b,d.

Table 7. Emission mechanisms of the SRO films.

Position	Mechanisms of Emission
From 1.77 to 1.24 eV Infrared [3,13]	(CLI) Luminescent centers located in the nc-Si/SiO ₂ Interface
From 1.99 to 1.77 eV Red [13,17]	(QC) Quantum Confinement effect with the interaction of the nc-Si interface and the oxide matrix.
From 2.2 to 1.99 eV Orange and Red [13,31]	(NBOHC) and E' centers ≡Si–O•O≡Si+ Non-Bridge Oxygen Hole Center
From 2.51 to 2.07 eV Green and Yellow [3,13,31]	(Eδ') Positively charged Oxygen vacancies
From 2.72 to 2.51 eV Blue [3,13,17]	(NOV) (O ≡Si-Si ≡O) Neutral oxygen Vacancies
From 3.17 to 2.72 eV Violet [3,13,31]	(WOB) Weak Oxygen Bonds

In Table 6, it is described quantitatively the area percentage under the curve (A_T) of the photoluminescent intensity of each as-G and HT film, in order to know which film has the highest PL intensity. The Q/SRO_{25/100} film HT was taken as a reference since it had the highest PL intensity placing it at 100%. The observations were the films that showed a higher PL intensity, which was those with heat-treated and deposited on the Quartz substrate, because they provided some properties that favored the formation of the QC with an interaction of the Si-ncs-oxide matrix interface, for this reason, the PL intensities were located in the red and near-infrared bands; another observation was that the hydrogen flux at the 25 sccm level led to better results than the one at 100 sccm level, even in twofold-layers. It should also be noted that the good response of the PL intensity was because the films were thicker, which increased the number of defects and Si-ncs, which were found in the twofold-layers.

4. Discussion

The as-G SRO-HFCVD films, forming the one layer and twofold-layers structures, deposited on Q and Si substrate, according to the spectroscopic characterizations, had a thickness of $\approx 329 \pm 6$ nm with a refractive index of $\approx 2.245 \pm 0.21$ and a silicon excess of $10.25\% \pm 0.35\%$. It was found that for HT films the thickness decreased to $\approx 303.5 \pm 7.5$ nm, likewise the refractive index to ≈ 1.3 , and the silicon excess also decreased to $\approx 5.25\% \pm 0.25\%$. This clearly indicates that the thermal treatment at high temperature-induced the diffusion and nucleation of the Si atoms in excess, and with long times of the treatment the formation of the Si-ncs was also induced; this event could be explained by the Ostwald Maturation [34], which predicts that Si clusters grow larger when smaller Si clusters get together. As a result, the larger Si-ncs were formed in the SiO₂ matrix resulting in the decrease of Si aggregates. In regards to the Si-H bonds, they appeared in greater quantities in the as-G SRO films and were completely desorbed in HT films. Therefore, the Si-ncs size depended on the concentration of the Si atoms excess (clusters) and the duration of the thermal treatment. It should be noted that the results of the refractive index, silicon excess, and vibrational modes could be obtained from the optical of these SRO films. It results that in the as-G films the silicon excess was higher, the refractive index was higher, and the FTIR spectra were of lower intensity than for those obtained in the HT SRO films. Conversely, with HT the silicon excess and refractive index decreased, but the FTIR spectra increased their intensity, this indicates a better stoichiometry of the material. Furthermore, taking into account the aforementioned, it was confirmed that the PL spectra observed in both a single-layer and twofold-layer as-G films were of weak intensity because both the refractive index and the silicon excess were higher, but for the HT films the refractive index and silicon excess, the PL intensity was increased due to the Si-ncs formation and oxygen-related defects. As for the FTIR spectra of the as-G films, they show the vibrational modes Si-OH, Si-O, and OH, which were part of the defects related to the oxygen mentioned in the PL also in the as-G SRO films, which allowed us to corroborate the existence of these defects, as in the previous cases, in the HT films there was a modification of these FTIR spectra in which we could observe the disappearance of the vibration mode of inflection, bending, and stretching of Si-H attributed to the Hydrogen. The absorption edge of the transmittance spectra of the HT films moved to shorter wavelengths regions, as a result of the restructuring of the material reaching a stable phase

and the decrease of silicon excess in the films. According to Zacharias reports [21] when decreasing silicon excess, Si-ncs with smaller size are obtained, which is corroborated by using HRTEM analysis from which well-formed Si-ncs are observed having a 2.3 ± 0.6 nm average size. The different sizes are compared with those obtained by theoretical calculations in which the $E_{g_{opt}}$ is used. The latter is obtained by the Tauc method and by using the highest peak value in the PL spectra, the average sizes of the Si-ncs are found corresponding to 1.75 ± 0.105 nm and 1.645 ± 0.015 nm, respectively, which are values close to each other.

Another point to highlight is related to the substrates in which the films are deposited since according to Table 6, the best responses in photoluminescent intensity were observed in the HT films deposited on Q; as to the films as-G it was observed that the film deposited on Si substrate exhibited a PL intensity, which was slightly higher than that emitted by the film deposited on the Q substrate, although such intensity was less than that of the HT film by an order of magnitude. In respect to the twofold-layer structures, the twofold-layer film Q/SRO_{25/100} HT was the one that shows the best photoluminescent intensity.

5. Conclusions

The SRO-HFCVD films were deposited on Quartz and Silicon substrates considering two Hydrogen fluxes at levels of 25 and 100 sccm holding the source-substrate distance fixed at 8 mm, under these conditions the single-layer SRO₂₅, SRO₁₀₀, and twofold-layer SRO_{25/100} and SRO_{100/25} films as-G and HT were grown. All the as-G SRO films were thicker than the HT SRO-films as was corroborated by null ellipsometry. The refractive index of the single-layer HT films decreased; on the other side, for the corresponding twofold-layer, it increased due to the restructuring of the material. The FTIR spectra showed the typical SiO₂ bonds. In addition, the SRO films as-G showed three characteristic vibrational modes due to the hydrogen bonds such as inflection, bending, and stretching modes. After applying heat treatment, the FTIR spectra shifted to regions of higher wavenumber, indicating that a structural rearrangement occurred in the material, as well as the desorption of Hydrogen. Besides, the heat-treated induced the phase separation of Si and SiO₂, allowing the material to restructure. By means of the transmittance spectra were obtained the optical bandgap energies ($E_{g_{opt}}$) ranging from 2.2 to 3.25 eV, such values are dependent on whether the film is as-G or HT. The Si-ncs diameter was estimated by using both the $E_{g_{opt}}$ and PL peaks. The absorption coefficient obtained from the transmittance underwent a shift to shorter wavelengths after applying HT, as a consequence of the material restructuring. On the other hand, the PL spectrum of the as-G single-layer films exhibited two characteristic emission bands, the blue and red bands with a higher PL emission in the blue one, the blue band is attributed to luminescent centers between 2.5 and 3 eV (blue-violet) and the red one to Si-ncs. As to the as-G twofold-layers films, the PL spectra had a broader spectrum ranging from 1.77 to 3.5 eV (red to violet), and their PL intensity was higher than those of the single-layer films. In the films with HT, the best PL spectra were obtained, the single-layer and twofold-layer films PL spectra showed two emission peaks, one located in 3 eV (Violet region), and the other with greater intensity and wider PL peak, located between 1.5 and 2 eV (orange to near-infrared region). It should be noted that the best and highest PL intensity was obtained in the twofold-layer film Q/SRO_{25/100}. In addition, the cross-sectional profile of the Si/SRO₂₅/SRO₁₀₀ films was obtained by Scanning Electron Microscopy, which corroborated the deposit of the two layers, as well as the thickness of the films. Through the analysis from the images obtained by HRTEM transmission, it was also possible to corroborate the Si-ncs size. Besides, the Si-ncs size was also estimated in a theoretical form resulting similar to that obtained by HRTEM, where this comparison confirms both results.

Author Contributions: H.P.M.H. designs the experiments and carried out some characterizations besides writing. J.A.L.L. designs the experiments, writing-review, J.Á.D.H.d.l.L., A.L.F., K.M.L., G.G.S., R.O.F., S.A.P.G., R.R.A., and, J.C.L. writing-review and critical review, Z.J.H.S., and, G.O.M.C. some characterizations. All authors have read and agreed to the published version of the manuscript.

Funding: This research received no external funding.

Acknowledgments: This work has been partially supported by CONACyT-CB-255062 and VIEP-LULJ-EXC-2019. The authors acknowledge CIDS, IFUAP laboratories for their help in the sample's characterizations.

Conflicts of Interest: The authors declare no conflict of interest.

References

1. DiMaria, D.J.; Dong, D.W.; Theis, T.N.; Kirtley, J.R.; Tsang, J.C.; Young, D.R.; Pesavento, F.L. Charge transport and trapping phenomena in off-stoichiometric silicon dioxide films. *J. Appl. Phys.* **1983**, *54*, 5801–5827. [[CrossRef](#)]
2. Canham, L.T. Silicon quantum wire array fabrication by electrochemical and chemical dissolution of wafers. *Appl. Phys. Lett.* **1990**, *57*, 1046. [[CrossRef](#)]
3. Morales-Sánchez, A.; Leyva, K.M.; Aceves, M.; Barreto, J.; Domínguez, C.; Luna-López, J.A.; Carrillo, J.; Pedraza, J. Photoluminescence enhancement through silicon implantation on SRO-LPCVD films. *Mater. Sci. Eng. B* **2010**, *174*, 119–122. [[CrossRef](#)]
4. Lin, Z.; Guo, Y.; Song, J.; Zhang, Y.; Song, C.; Wang, X.; Huang, R. Effect of thermal annealing on the blue luminescence of amorphous silicon oxycarbide films. *J. Non-Cryst. Solids* **2015**, *428*, 184–188. [[CrossRef](#)]
5. Cabañas-Tay, S.A.; Palacios-Huerta, L.; Aceves-Mijares, M.; Coyopol, A.; Morales-Morales, F.; Pérez-García, S.A.; Licea-Jiménez, L.; Domínguez-Hornad, C.; Monfil-Leyva, K.; Morales-Sánchez, A. Study of narrow and intense UV electroluminescence from ITO/SRO/Si-p and ITO/SRN/SRO/Si-p based light-emitting capacitors. *J. Lumin.* **2017**, *183*, 334–340. [[CrossRef](#)]
6. Pandey, R.K.; Patil, L.S.; Bange, J.P.; Patil, D.R.; Mahajan, A.M.; Patil, D.S.; Gautam, D.K. Growth and characterization of SiON thin films by using the thermal-CVD machine. *Opt. Mater.* **2004**, *25*, 1–7. [[CrossRef](#)]
7. Hsieh, C.-R.; Chen, Y.-Y.; Lou, J.-C. Effect of fluorinated silicate glass passivation layer on electrical characteristics and dielectric reliabilities for the HfO₂/SiON gate stacked nMOSFET. *Microelectron. Eng.* **2010**, *87*, 2241–2246. [[CrossRef](#)]
8. Luna López, J.; Carrillo López, J.; Aceves Mijares, M.; Morales Sánchez, A.; Falcony, C. FTIR and photoluminescence of annealed silicon-rich oxide films. *Superficies Vacío* **2009**, *22*, 11–14.
9. González Fernández, A.A. MOS-like electroluminescent devices using silicon-rich oxide obtained by LPCVD. In Proceedings of the 2009 6th International Conference on Electrical Engineering, Computing Science and Automatic Control (CCE), Toluca, Mexico, 10–13 January 2009.
10. Benítez-Lara, A.; García-Salgado, G.; Vázquez-Valerdi, D.E.; Morales-Sánchez, A.; Espinosa-Torres, N.D.; Luna-López, J.A. Silicon rich oxide powders by HWCVD: Its optical and morphological properties. *Adv. Powder Technol.* **2015**, *26*, 163–168. [[CrossRef](#)]
11. Valerdi, D.E.V.; López, J.A.L.; Salgado, G.G. Twofold SiO_x Films deposited by HFCVD: It is Optical, Compositional and Electrical Properties. *Procedia Eng.* **2014**, *87*, 168–171. [[CrossRef](#)]
12. Hernández Simon, Z.J. Propiedades Fotovoltaicas de Películas SRO depositadas mediante HFCVD en Estructuras ITO/SRO/Si y AU/SRO/Si. Master's Thesis, Benemérita Universidad Autónoma de Puebla (BUAP), Puebla, Mexico, 2018.
13. Mendoza Conde, G.O. Propiedades fotoeléctricas de películas de SRO depositadas mediante HFCVD en estructuras Au/SRO/Si. Master's Thesis, Benemérita Universidad Autónoma de Puebla (BUAP), Puebla, Mexico, 2018.
14. Chávez Velázquez, R.; Zaldivar Huerta, I.; Reyes Betanzo, C.; Díaz Sánchez, A. Fabricación de guías de onda ópticas en silicio utilizando óxido de silicio y nitruro de silicio. *Superf. Vacío* **2005**, *18*, 21–23.
15. Luna-López, J.A.; García-Salgado, G.; Díaz-Becerril, T.; López, J.C.; Vázquez-Valerdi, D.E.; Juárez-Santiesteban, H.; Rosendo-Andrés, E.; Coyopol, A. FTIR, AFM and PL properties of thin SiO_x films deposited by HFCVD. *Mater. Sci. Eng. B* **2010**, *174*, 88–92. [[CrossRef](#)]
16. Philipp, H.R. Optical and bonding model for non-crystalline SiO_x and SiO_xN_y Materials. *J. Non Cryst. Solids* **1972**, *8–10*, 627–632. [[CrossRef](#)]
17. Chen, X.Y.; Lu, Y.F.; Tang, L.J.; Wu, Y. H Annealing and oxidation of silicon oxide films prepared by plasma-enhanced chemical vapor deposition. *J. Appl. Phys.* **2005**, *97*, 1–10. [[CrossRef](#)]
18. Quiroga-González, E. On the photoluminescence of multilayer arrays of silicon-rich oxide with high silicon content prepared by low-pressure chemical vapor deposition. *Thin Solid Film.* **2011**, *519*, 8030–8036. [[CrossRef](#)]

19. Sitarz, M. The structure of simple silicate glasses in the light of Middle Infrared spectroscopy studies. *J. Non Cryst. Solids* **2011**, *357*, 1603–1608. [[CrossRef](#)]
20. Tomozeiu, N. Silicon Oxide (SiO₂): A Challenging Material for Optoelectronics. In *Optoelectronics-Materials and Techniques*; IntechOpen: London, UK, 2011; Chapter 3; pp. 55–98.
21. Morales-Sánchez, A. Optical characterization of silicon-rich oxide films. *Sens. Actuators Phys.* **2008**, *142*, 12–18. [[CrossRef](#)]
22. Flores Gracia, F. Photoluminescence and cathodoluminescence characteristics of SiO₂ and SRO films implanted with Si. Superficies y vacío. In *Sociedad Mexicana de Ciencia y Tecnología de Superficies y Materiales A.C.*; Distrito Federal: Mexico City, Mexico, 2005; Volume 18, pp. 7–13.
23. Koshida, N. *Device Applications of Silicon Nanocrystals and Nanostructures*; Springer Science & Business Media: Berlin/Heidelberg, Germany, 2008.
24. Zacharias, M.; Heitmann, J.; Scholz, R.; Kahler, U.; Schmidt, M.; Bläsing, J. Size-controlled highly luminescent silicon nanocrystals: A SiO/SiO₂ superlattice approach. *Appl. Phys. Lett.* **2002**, *80*, 661. [[CrossRef](#)]
25. Álvarez, M.P.; Carreras, J.; Barreto, J.; Morales, A.; Domínguez, C.; Garrido, B. Efficiency and reliability enhancement of silicon nanocrystal field-effect luminescence from nitride-oxide gate stacks. *Appl. Phys. Lett.* **2009**, *92*, 241–104.
26. Berencén, Y.; Ramírez, J.M.; Jambois, O.; Domínguez, C.; Rodríguez, J.A.; Garrido, B.J. Rare Earth-Doped Silicon-Based Light Emitting Devices: Towards new Integrated Photonic Building Blocks. *Appl. Phys.* **2012**, *112*, 022–114.
27. Adams, A.C. Plasma Deposition of Inorganic Films. *Solid State Technol.* **1983**, *26*, 135–139.
28. Tauc, J. Optical Properties and Electronic Structure of Amorphous Germanium. *Phys. Status Solidi* **1966**, *15*, 627. [[CrossRef](#)]
29. Keinonen, J.; Djurabekova, F.; Nordlund, K. *Silicon Nanophotonics Basic Principles, Present Status and Perspectives*; Pan Stanford Publishing: New York, NY, USA, 2009; pp. 379–394.
30. Sattler, K. *Encyclopedia of Nanoscience and Nanotechnology: Silicon Nanowires*; American Scientific Publishers: Valencia, CA, USA, 2004; Volume 9, pp. 815–835.
31. Kwon, Y.H.; Park, C.J.; Lee, W.C. Memory effects to deep levels in metal-oxide-semiconductor structure with nanocrystalline Si. *Appl. Phys. Lett.* **2002**, *80*, 2502–2504. [[CrossRef](#)]
32. Wang, Y.; Townsend, P.D. Common mistakes in luminescence analysis. *J. Physics. Conf. Ser.* **2012**, *398*, 012003. [[CrossRef](#)]
33. Jaeger, R.C. *Introduction to Microelectronic Fabrication*; Addison-Wesley Publishing: Boston, MA, USA, 1990.
34. Hung-Yu, T.; Chiao-Ti, L.; Lin-Hsuan, T.; Yung-Hsian, L.; Yi-Hao, P.; Chih-I, W.; Gong-Ru, L. SiC and Si Quantum Dots Co-Precipitated Si-Rich SiC Film with n- and p-Type Dopants Grown by Hydrogen-Free PECVD. *ECS J. Solid State Sci. Technol.* **2013**, *2*, N159–N164.

